EAI Endorsed Transactions
on Sustainable Manufacturing and Renewable Energy Research Article EAI.EU

Design and Implementation of a Line-Tracking Robot for Autonomous Navigation

L. H. Huynh [1], D. T. Duong[1] and V. Lourve[1,*]

[1] Grenoble Alpes University, France

Abstract

This study presents the design and implementation of a line-following Automated Guided Vehicle (AGV) for stock distribution using color detection. The AGV incorporates mechanical, electrical, and control engineering principles to improve warehouse automation. The primary goal is to develop an AGV that autonomously follows a designated path and sorts stocks by color. This project enhances students' understanding of mechatronics system design by integrating fabrication, sensor integration, embedded programming, and control system optimization. The methodology includes system modeling, hardware selection, circuit design, algorithm implementation, and experimental validation. The AGV's performance was assessed under different conditions to evaluate accuracy, stability, and adaptability. The AGV successfully follows predefined paths and accurately classifies stocks by color, optimizing logistics and automation processes. Experimental and simulation data confirm the system's effectiveness. This project establishes a fundamental framework for AGV-based logistics and contributes to the advancement of autonomous warehouse solutions.

Keywords: Line-tracking robot, autonomous navigation, colour detection, embedded systems, mechanical engineering

Received on 29 March 2025, accepted on 08 August 2025, published on 08 August 2025

doi: 10.4108/eetsmre.8988

1. Introduction

1.1 Background

Automation and robotics are essential components of modern engineering [1-3], enabling industries to optimize processes, reduce labor dependency, and improve operational efficiency. Line-tracking robots as Fig. 1 play a crucial role in these advancements, particularly in logistics, manufacturing, and smart infrastructure applications. The ability of mobile robots to follow predetermined paths autonomously has significant implications for material handling, smart transportation, and industrial automation.

This study focuses on designing and developing a line-tracking robot that navigates a predefined path based on color recognition. The project aims to equip students with practical experience in mechanical design, electrical systems, programming, and control logic. The integration of these disciplines helps develop problem-solving skills and prepares students for future careers in automation and robotics.

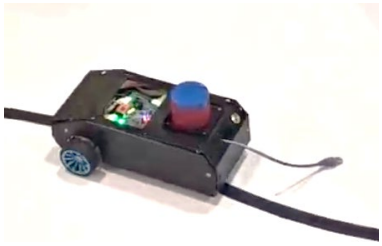

Figure 1. Overview of the robot line-tracking.

*Corresponding author. Email: lourve.vincent@gmail.com

1.2. Objectives

The primary objectives of this study are to design and construct a mobile robot capable of autonomous navigation, develop an effective color-based line-tracking algorithm [4, 5] for accurate path following, integrate mechanical, electrical, and software components into a cohesive and functional system, evaluate the robot's performance under varying environmental conditions, and provide students with practical, hands-on experience in system integration and engineering problem-solving.

2. Mechanical Design

2.1. Structure Overview

The construction of the mechanical structure plays an extremely significant role. It affects the distribution of the structure, the structure of the electrical system and the programming part of the AGV. Mechanical design defines the necessary conditions of the vehicle structure to meet the specified requirements, determine the AGV sizes, as well as the motor parameters. Besides, it is also used to analyse and model the system dynamic.

From the analysis and selection of viable options presented in Fig. 2, it shows the general structure of AGV with two driving wheels controlled by two separate motors and simultaneously drive multi-directional auxiliary wheels (caster) placed behind the AGV to balance the system. For a load stock AGV, its speed shall not exceed 0.3 m/s to ensure safety issues [6]. Therefore, 0.3 m/s is chosen as the normal velocity of the entire AGV, maximum velocity is $0.3\,m/s$ and angular velocity is $0.6\,rad/s^2$. The smallest curve radius is 500 mm.

2.2. Important parameters

The important parameters considered in the mechanical design include the distance between the two front driving wheels W (mm), the radius of each driving wheel r (mm), and the height of the center of gravity h (mm). Additionally, the object placement location is defined by two key distances: a_1 (mm), which is the distance from the front driving wheel axis to the object's center of gravity, and a_2 (mm), which is the distance from the object's center of gravity to the castor wheel.

2.3. Mechanical constraint

Roll over condition

To ensure stability and prevent rollover, the design considers typical ratios observed in existing mobile robot models [7, 8] such as the Pioneer 3DX and Heros Robot, where the ratio between the distance from the driving wheel axis to the castor wheel and the distance between the two driving wheels ranges from 1 to 1.5. Based on this, a ratio of 1.25 is selected. Accordingly, the AGV's length is chosen as L=1.25×W, where W is the distance between the front driving wheels. The rollover condition during deceleration is analysed using the vehicle's dynamic model.

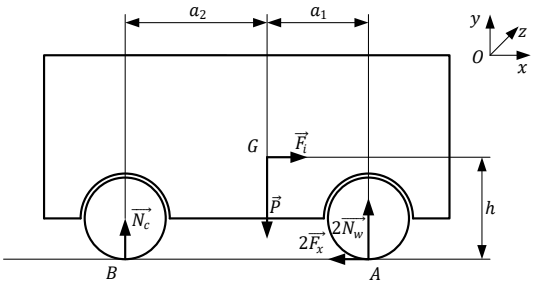

Figure 2. Roll over condition when decelerating.

Based on Newton's 2nd law and equilibrium equations, we have the system of vehicle dynamics equations as below,

$$\begin{cases} \Sigma\vec{F_x} = \vec{0} \\ \Sigma\vec{F_y} = \vec{0} \\ \Sigma\vec{M_{\frac{z}{A}}} = \vec{0} \end{cases} \Leftrightarrow \begin{cases} 2F_x = F_i \\ 2N_w + N_c = mg \\ N_c(a_1 + a_2) = Pa_1 - F_i h \end{cases} \quad (1)$$

The normal forces at each wheel are:

$$\begin{cases} N_c = mg\dfrac{a_1}{a_1 + a_2} - ma\dfrac{h}{a_1 + a_2} \\ N_w = \dfrac{1}{2}\left(mg\dfrac{a_2}{a_1 + a_2} + ma\dfrac{h}{a_1 + a_2}\right) \end{cases} \quad (2)$$

Condition for the AGV does not roll over when decelerating, the normal force at castor wheel must satisfy:

$$N_c \geq 0 \quad (3)$$

Which can be rewritten as:

$$\begin{aligned} Pa_1 &\geq F_i h \\ mga_1 &\geq mah \\ \Rightarrow a_1 &\geq h\frac{a}{g} \end{aligned} \quad (4)$$

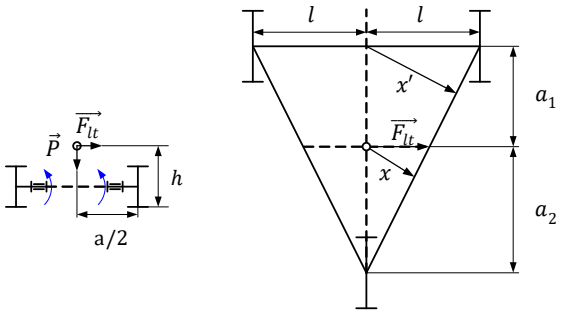

Figure 3. Roll over condition when turning

Prevent diagonal rollover condition:

$$Px \geq F'_{lt}h \quad (5)$$

Where x can be determined as equation below:

$$(a_1 + a_2)l = x'\sqrt{(a_1 + a_2)^2 + l^2}$$

$$\Rightarrow x' = \frac{(a_1 + a_2)l}{\sqrt{(a_1 + a_2)^2 + l^2}} \quad (6)$$

And F'_{lt} is:

$$F'_{lt} = F_{lt}\frac{x'}{l} = F_{lt}\frac{a_1 + a_2}{\sqrt{(a_1 + a_2)^2 + l^2}} \quad (7)$$

Apply equations (6) and (7) into (5), the inequation can be rewritten as:

$$mg\frac{a_2 l}{\sqrt{(a_1 + a_2)^2 + l^2}} \geq F_{lt}\frac{a_1 + a_2}{\sqrt{(a_1 + a_2)^2 + l^2}}h$$

$$mga_2 l \geq F_{lt}(a_1 + a_2)h$$

$$\Rightarrow a_2 \geq 2.5\frac{v^2}{R}\frac{h}{g} \quad (8)$$

Where: P is gravitation; F_i is the inertial force; F_{lt} is centrifugal force of the entire AGV; F'_{lt} centrifugal force of the entire AGV on x axis.

Acceleration setup

The acceleration and velocity can be related by the equation:

$$v^2 - v_0^2 = 2as \quad (9)$$

Where:

s: Is the distance the AGV to go after cannot detect line.

In this case, let consider acceleration of the AGV equal the acceleration to stop in the end of the line path. Preliminary select the value of these AGV parameter by using constraints above, the stopping distance is $s = 65\ mm = 0.065\ m$.

From the stopping distance and the desired speed, the acceleration can be calculated as follow:

$$a = \frac{v^2 - v_0^2}{2s} = \frac{0^2 - 0.3^2}{2 \times 0.065} \approx 0.69\ (m/s^2)$$

Choose the AGV acceleration $a = 0.69\ m/s^2$

Table 1.
Preliminary select parameter

Parameter	Symbol	Value
The distance between two front driving wheels	W	182 mm
The Radius of driving wheel	r	32.5 mm
The height of the center of gravity	h	63 mm
The distance between driving wheel axis and the bottom edge of the sensor module	l	90 mm
The distance between the front driving wheel axis and the center of gravity of the object	a_1	59 mm
The distance between the object's center of gravity to the castor wheel	a_2	147 mm

Check condition

From Table 1, we substitute these values into inequation (4) and (8):

$$a_1 \geq h\frac{a}{g}$$

$$\Rightarrow a_1 = 59 \geq 63 \times \frac{0.69}{9.81} \geq 4.43$$

$$a_2 \geq 2.5\frac{v^2}{R}\frac{h}{g}$$

$$\Rightarrow a_2 = 147 \geq 2.5 \times \frac{0.3^2 \times 63}{0.0325 \times 9.81} \geq 44.46$$

Both inequations are satisfy.

Wheel calculation and motor

Input

- Maximum velocity: v=0.3 m/s
- Acceleration: a=0.5 m/s^2
- Wheel radius r=32.5 mm
- Wheel weight: 0.06 kg
- Estimate weight of entire AGV when loading: 4.5 kg
- Friction coefficient: =0.7
- Safety factor: =1.5

Force acting on wheel analysis.

- N_{castor}: Normal force acting on castor wheel.
- N_{Dw}: Normal force acting on each driving wheel.

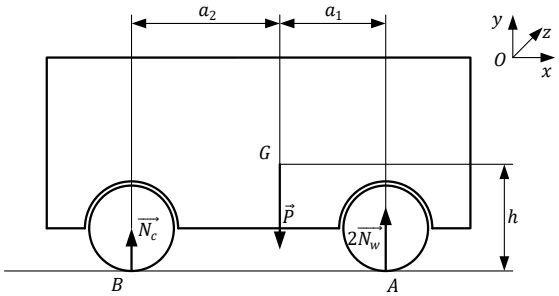

Figure 4. Force acting analysis.

In Fig. 4, balancing the vertical force equation

$$P = 2N_w + N_C \quad (10)$$

Balance Torque equation

$$2N_w a_1 = N_C a_2$$

$$\Rightarrow N_C = 2N_w\frac{a_1}{a_2} \quad (11)$$

Substitute N_C to force equation (10):

$$P = 2N_w + 2N_w \frac{a_1}{a_2}$$

$$\Rightarrow N_w = \frac{P}{2\left(1 + \frac{a_1}{a_2}\right)} \quad (12)$$

Substitute the preliminary parameter into equation (12), the normal force on the driving wheel can be calculated:

$$N_w = \frac{4.5 \times 9.81}{2\left(1 + \frac{59}{147}\right)} = 15.751\ (N)$$

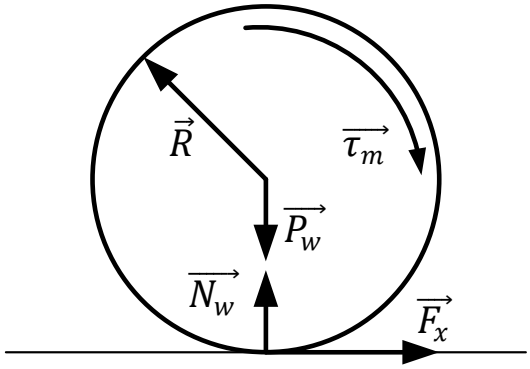

Figure 5. Wheel forces analysis.

The wheel inertial moment can be simplified as follow:

$$I = \frac{1}{2}mR^2 \quad (13)$$

The driving force apply on the driving wheel to obtain the acceleration $a = 0.69\ m/s^2$ is:

$$F = ma = (4.5 + 0.06) \times 0.69 = 3.146\ (N)$$

The wheel as Fig. 5 has to satisfy the non-slip condition, which is:

$$F_x \leq \mu N_w \quad (14)$$

Substitute all the value into inequation above:

$$F_x \leq \mu N_w$$

$$\Rightarrow F_x = 3.146 \leq 0.7 \times 15.751 \leq 11.02$$

The non-slip condition is satisfied.

Moment balancing equation for rotational motion:

$$\tau - F_x R = I\gamma$$

$$\Leftrightarrow \tau = F_x R + I\gamma$$

$$\Leftrightarrow \tau = F_x R + \frac{1}{2}mR^2\gamma$$

$$\Leftrightarrow \tau = F_x R + \frac{1}{2}mRa$$

$$\Rightarrow \tau = 3.146 \times 0.0325 + \frac{1}{2} \times 0.06 \times 0.0325 \times 0.69$$

$$\Rightarrow \tau = 0.1029\ (Nm)$$

The necessary moment at the drive wheel is:

$$\tau_m \geq SF\tau = 1.5 \times 0.1029 = 0.1544\ (Nm)$$

Where: $SF = 1.5$ is safety factor.

Number of revolutions of the motor:

$$n_m \geq \frac{60 v_{max}}{2\pi R} = \frac{60 \times 0.3}{2 \times 3.14 \times 0.0325} = 88.19\ (rpm) \quad (15)$$

The wheels angular velocity is:

$$\omega = \frac{2\pi}{60} n_m = \frac{2 \times 3.14}{60} \times 88.19 = 9.23\ (rad/s) \quad (16)$$

Power of the motor:

$$P_m = \tau_m \times \omega = 0.1544 \times 9.23 = 1.425\ (W) \quad (17)$$

The necessary parameters the chosen motor need to be satisfied are: Minimum torque of motor: $\tau_m \geq 0.1544\ Nm$; Minimum number of revolutions of motor: $\omega \geq 88.19\ rpm$. DC motors are used widely for wheels mobile robot because this type of motors can achieve fast speed, large torque when running at low speed and continuous rotation until the power is cut off, besides it is also possible to combine with some controllers to precisely adjust the speed of the motor by integrated speed sensors. However, this type of motors works poorly in low-speed areas, and some motors still have dead bands in this speed range.

In addition, there are servo and stepper motors that are often used in models with high requirements for precise position control, large torque, and constant holding torque without using a starter motor. In the servo system, it uses feedback loop mechanism to control the position, but the rotation angle is limited from 0° ÷ 180° or lower, when the start command to rotate, the motor will move to the correct position and stay the same there even when an external force acts on it. From the typical characteristics of the above motor types, DC electric motors are used to deploy the system.

Based on the requirements stated above, DC motor $JGA25$ is choosen, the specifications of the selected motor for driving the wheels are shown in Table 2.

Table 2.
Jga25 parameters

Parameters	Value
Rated power	$6\ W$
Angular velocity	$130\ rpm$
Number of pulses encoder	11
Voltage	$12\ V$
Max current	$0.5\ A$

Load simulation on the covers

In Fig. 6 and Fig. 7, our simulation is conducted on SolidWorks Simulation, with 2kg load. The maximum displacement at the load position is approximately 0.05mm, which is acceptable and does not much to the color sensor.

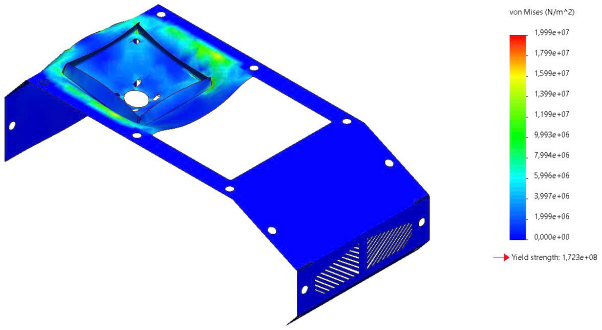

Figure 6. Stress distribution on the covers.

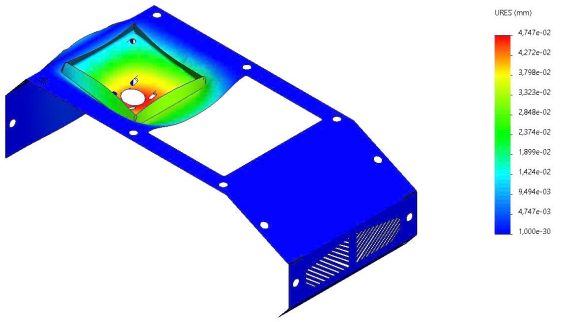

Figure 7. Displacement on the covers

Coaxial crafting

First, we will assemble the flange and the reference surface part. The reference surface will first placed on the table, then we will turn up-side down the flanges and place it next to the side face of the surface component, which will create a flat plane due to the titration of the table. Then, we will use the super-flat surface block to hold the side face of two parts, which will create another flat plane on the side surface.

Then, we will stick two parts together by screws through the top holes of flanges, which is on the straight-line with the side holes of reference surface. The crafted part will now provide a new flat surface, and two side center holes will also stay on a straight-line due to the titration of the table, which will ensure the coaxial of motors.

After that, we will attach the motors with bearings, which will be in charge of loading the entire AGV, and pledge it to the inside surface of crafted part. The motor shaft will now attach the coupling, which help connecting the tire and the shaft. According to the titration of side surfaces, the motor shafts will now ensure the coaxial, the tires will now stay on the same plane.

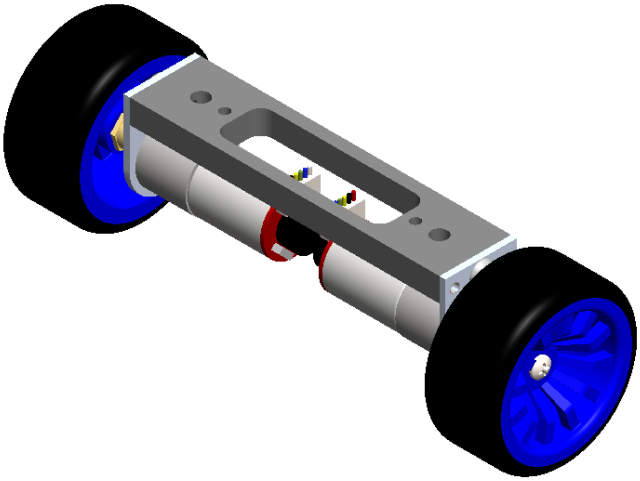

Figure 8. Coaxial crafting

3. Electrical Design

3.1 Principle Diagram

Figure 9 illustrates the overall hardware architecture and signal flow of the autonomous line-tracking robot. At the centre of the system is the microcontroller block, which acts as the brain of the AGV, managing all sensor inputs and actuator outputs. The microcontroller receives signals from five line-tracking sensors responsible for detecting the predefined path, as well as from a colour sensor used to identify and classify stocks based on colour. Additionally, it interfaces with a start button and a limit switch for user control and safety.

For locomotion, the microcontroller sends PWM and direction control signals to the left and right motor drivers, which in turn drive the left and right DC motors, respectively. Each motor is equipped with an encoder that feeds back real-time speed and position data to the microcontroller, enabling closed-loop control. The power architecture is divided into two subsystems: a control power line and a dynamic power line. The control power, regulated through a 3.3V buck converter, supplies low-voltage components like the microcontroller and sensors. Meanwhile, the motors and their drivers draw power from a 12V buck converter connected to a dedicated dynamic power source. Solid lines in the diagram represent power lines, while dashed lines indicate signal lines. This separation ensures clean power delivery and noise isolation between control and actuation systems. Overall, the diagram demonstrates a well-organized and modular approach to integrating sensors, actuators, and power systems in a compact robotic platform.

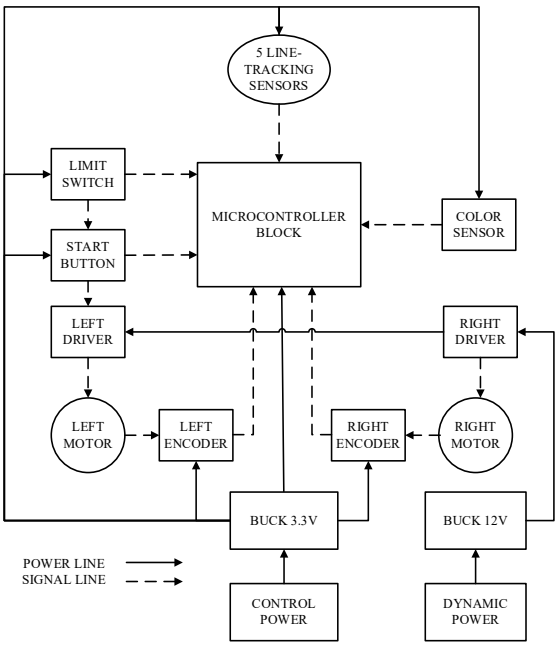

Figure 9. Circuit block diagram.

3.2. Electrical System

Microcontroller

There are different microcontrollers in the market, however, based on the problem statement, we chose the three most suitable microcontrollers as shown in Table 3: STM32F103C8T6, PIC16F877, and Atmega328P.

Table 3.
Advantages and disadvantages of microcontroller options

Type of micro-controller	ARM Cortex (STM32F103C8T6)	PIC(PIC16-F877)	ATMega (Arduino UNO)
Operating voltage	2V-3.6V	4V - 5.5V	~5V
Digital output	Have	Have	Have
Analog reading	Have analog read input	Have analog read input	Have analog read input
Commun-ication	Supports communicati on standards	Supports communica tion standards	Supports communicati on standards
	relay I2C, SPI, UART	relay I2C, SPI, UART	relay I2C, SPI, UART
Interrupt	Support modules external interrupt, timer…	Support modules external interrupt, timer…	Support modules external interrupt, timer…
Advan-tages	Compact, easy to install. Fast processing speed. Low price. The charging circuit is the same IDE, is diverse and easy to use.	Compact, easy to install. Low price. The charging circuit is the same IDE, is diverse and easy to use.	Compact, Easy to arrange. Full support library Inexpensive Analog input pins available Directly read sensor signals
Disadvan-tages	The number of analog channels is relatively limited	The number of analog channels is less than STM. Processing speed is slow	The number of analog channels is less than STM. Processing speed is slow

We have selected a centralized control structure as Fig. 10; a microcontroller will be used as the controller. The reasons for this choice are as follows:

- A centralized control structure simplifies programming by eliminating the need for inter-MCU communication. However, a sufficiently powerful controller is required to handle both algorithm processing, sensor data reading, and controlling peripheral modules.
- A microcontroller is chosen as the controller due to its high processing speed, which is sufficient for centralized control, and its compact size, making it suitable for mechanical systems.

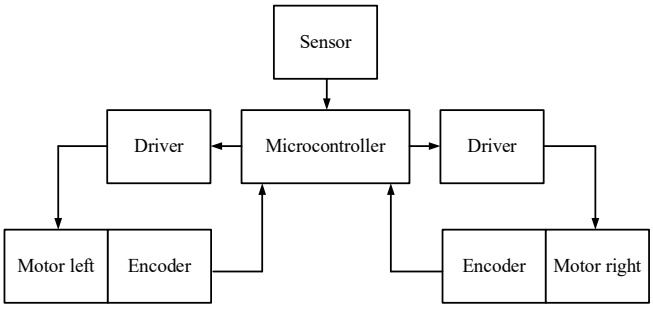

Figure 10. Control structure of the line follower robot

The chosen MCU should have sufficient I/O pins for interfacing with various sensors and actuators, and possess the processing power to execute the control algorithm. Specifically, the microcontroller must:

- Read digital values from 5 TCRT5000 sensors.
- Read values from TCS34725.
- Read encoder signals from the motors to calculate the actual vehicle speed.
- Generate PWM signals to control the motors.
- Based on the above requirements, our group has decided to use the STM32F103C8T6 Blue Pill microcontroller.

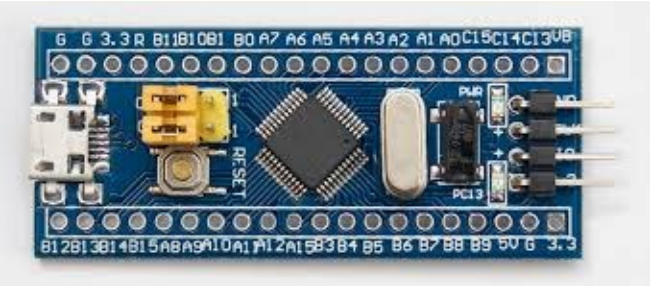

Figure 11. STM32F103C8T6 Blue Pill

In Fig. 11, specifications of the STM32F103C8T6 Blue Pill microcontroller are:

- Operating voltage 2.0V to 3.6V.
- Memory: 64KB Flash memory
- Internal quartz using RC oscillator in 8MHz or 40kHz mode.
- 2 ADC 12-bit units with 9 channels for each unit. Conversion ranges from 0 – 3.6V.
- 7 timers: 3 16-bit timers supporting IC/OC/PWM modes. 1 16-bit timer supporting motor control with protection modes such as input interrupts. 2 watchdog timers used for protection and error checking. 1 24-bit SysTick timer counting down used for applications like Delay function
- Full support for communication standards such as I2C, USART, SPI, CAN, USB 2.0
- SWD programming standard

Navigation Sensors

In this work, the navigation sensor plays a critical role in enabling the AGV to follow a designated path with precision. To select the most appropriate sensor for line tracking, a comparative analysis was conducted between three commonly used sensor types: camera, phototransistor, and photoresistor. As shown in Table 4, the comparison is based on four criteria: processing speed, accuracy, cost, and algorithm complexity. The camera offers high accuracy but is relatively slow and expensive, and its algorithm is complex. Meanwhile, phototransistors and photoresistors provide faster processing and simpler algorithms, though they are less accurate than cameras. Among the options, the phototransistor-based TCRT5000 sensor was selected for this study due to its balance between speed, simplicity, low cost, and adequate accuracy for the intended application.

Table 4.
Comparison table of line tracking sensor options

	Camera	Phototran-sistor	Photore-sistor
Processing Speed	Slow	Fast	Fast
Accuracy	High	Low	Low
Cost	High	Low	Low
Algorithm	Complex	Simple	Simple

The TCRT5000 is an integrated reflective optical sensor that combines an infrared emitter and a phototransistor in a single package. It is highly suitable for detecting variations in surface reflectivity, such as the contrast between black lines and a white background. Fig. 12 shows the structural diagram and pinout of the TCRT5000 sensor, including dimensions and orientation details necessary for mechanical integration into the robot platform. This compact size allows it to be easily mounted in an array configuration for enhanced positional accuracy during line tracking.

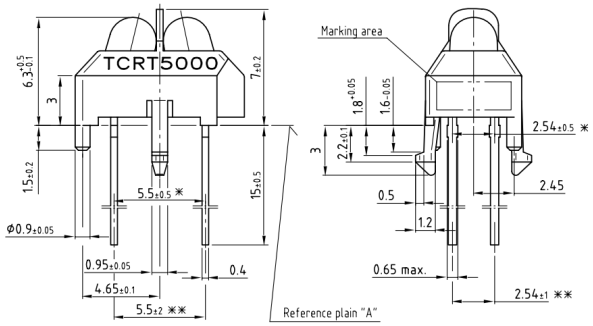

Figure 12. TCRT5000 sensor

Detailed specifications of the TCRT5000 sensor are summarized in Table 5. The sensor operates effectively within a working distance of 0.2 to 15 mm and emits infrared light at a wavelength of 950 nm. Its transmitter and receiver angles are both set at 10°, and the recommended forward current for the emitter LED is 100 mA. These characteristics make it well-suited for high-speed, real-time detection of lines, especially in controlled indoor environments.

Table 5.
Specifications of tcrt5000

Parameter	Value	Unit
Working distance	$0.1 - 15$	mm
Wavelength	940	nm
Transit angle	16	°
Receive angle	30	°
Current I_{Cmax}	100	mA

Determining resistance for sensor

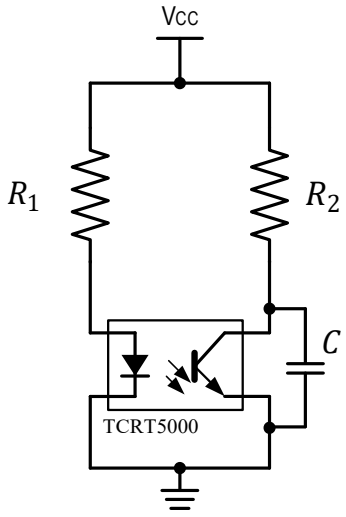

Figure 13. IR sensor module wiring diagram

We employ an RC low-pass filter as Fig. 13, with a resistor $R_2 = 4700\ \Omega$ and a capacitor $C = 10\ nF$, to mitigate the presence of undesired high-frequency signals in the microcontroller's signal input. The use of a low-pass filter is essential because it allows low-frequency components (such as the intended signal) to pass through while attenuating higher-frequency noise as Fig. 14 which could interfere with accurate readings.

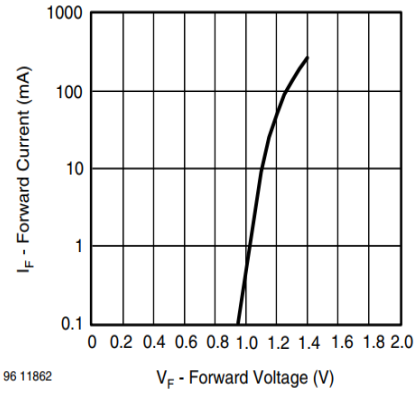

Figure 14. Forward current vs Forward voltage

Because the led works for a long time, we choose the current through the LED $I_F = 20(mA)$, resistor of LED:

$$R_1 = \frac{V_{CC} - V_F}{I_F} = \frac{5 - 0.9}{0.02} = 205\ \Omega \quad (18)$$

Choose resistor for led $R_1 = 220\ \Omega$

Position of sensor

In Fig. 15, the line is recognized if the line width is $d \geq X_d$. If the width is less than $\geq X_d$, the collector current change, $I_{c1} - I_{c2}$, that is the processable signal, becomes increasingly small and recognition increasingly uncertain. The switching distance or better its inverse can therefore be taken as a resolution of the sensor.

The switching distance, X_d, is predominantly dependent on the mechanical/ optical design of the sensor and the distance to the reflecting surface. It is also influenced by the relative position of the transmitter/ detector axis.

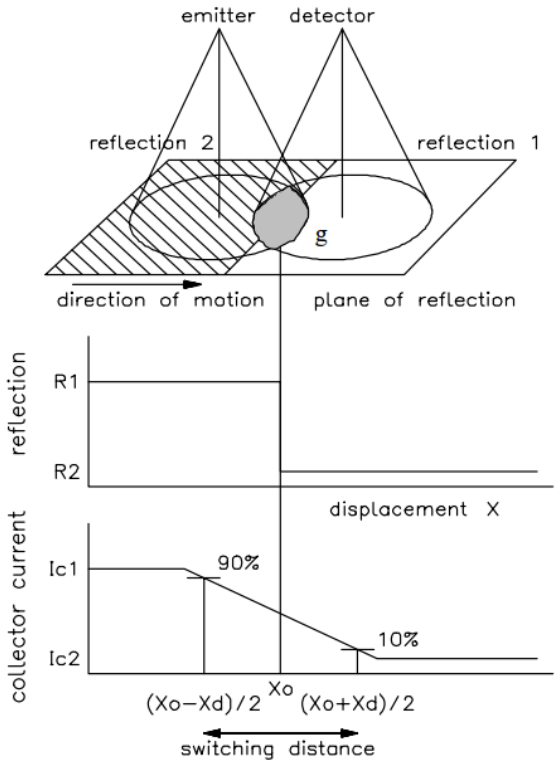

Figure 15. Abrupt reflection changes with associated Ic curve

The curves marked to position 1 in Fig. 16 correspond to the first position. The transmitter/ detector axis of the sensor was perpendicular to the separation line of the transition. In the second position (curve 2), the transmitter/detector axis was parallel to the transition. In the first position (1) all reflex sensors have a better resolution (smaller switching distances) than in position 2. It can recognize lines smaller than half a millimeter at a distance below 0.5 mm.

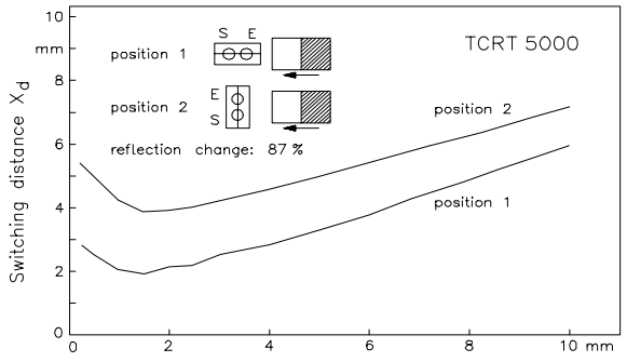

Figure 16. The switching distance as a function for the reflex sensors TCRT5000

4. Controller Design

4.1 Definition of Line Tracking and Error Identification:

For a freight-carrying AGV, successful line tracking requires minimizing the distance between the AGV's reference point and the centre of the line [9-11]. This goal ensures that the AGV remains accurately aligned with the path. To achieve this, two primary types of errors must be considered:

Lateral Error ($\boldsymbol{e_1}$): The deviation in the horizontal direction.

Longitudinal Error ($\boldsymbol{e_2}$): The deviation in the vertical direction.

Given the AGV's nonholonomic configuration—comprising two active wheels and one passive wheel—the AGV is constrained to motion in a single direction. Therefore, angular deviation ($\Delta\varphi$), the deviation between the AGV's movement direction and the tangent of the line at the reference point, should be a crucial factor in our controller.

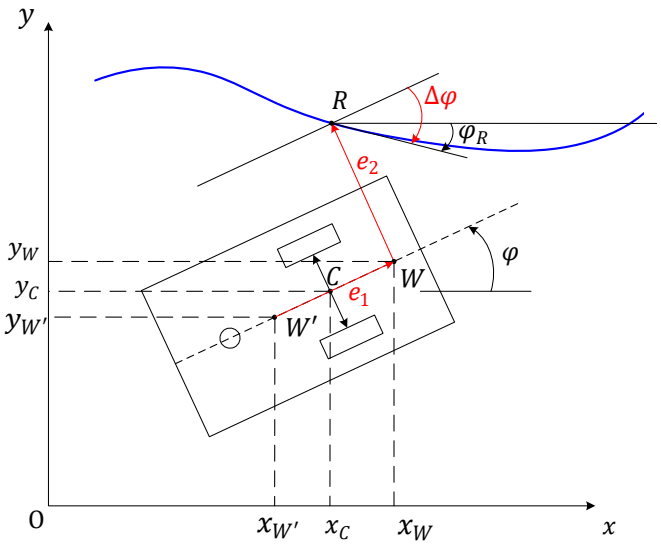

Figure 17. Error definition for controller

Let $R(x_R, y_R)$ represent the center of the line to be tracked. The following parameters are defined:

- φ_R: The angle between the tangent of the line at point R and the Ox-axis of the global coordinate system.
- e_1: The error between point R and point W' along the AGV's direction of movement.
- e_2: The error between point R and point W' perpendicular to the AGV's direction of movement.
- $\Delta\varphi$: The angular deviation between the AGV's direction of movement and the tangent of the line at point R.

Kinematic model and error calculations

The ordinary form of a mobile AGV with two actuated wheels can be derived as follows:

$$\begin{bmatrix}\dot{x}_C\\ \dot{y}_C\\ \dot{\varphi}_C\end{bmatrix}=\begin{bmatrix}\cos\varphi & 0\\ \sin\varphi & 0\\ 0 & 1\end{bmatrix}\begin{bmatrix}v_C\\ \omega_C\end{bmatrix} \quad (18)$$

And:

$$\begin{bmatrix}\omega_{Left}\\ \omega_{Right}\end{bmatrix}=\begin{bmatrix}\frac{1}{r} & -\frac{l}{r}\\ \frac{1}{r} & \frac{l}{r}\end{bmatrix}\begin{bmatrix}v_C\\ \omega_C\end{bmatrix} \quad (18)$$

We have that:

$$\begin{bmatrix}\dot{x}_{W'}\\ \dot{y}_{W'}\\ \dot{\varphi}_{W'}\end{bmatrix}=\begin{bmatrix}\cos\varphi & -d\sin\varphi\\ \sin\varphi & d\cos\varphi\\ 0 & 1\end{bmatrix}\begin{bmatrix}v_C\\ \omega_C\end{bmatrix} \quad (19)$$

A reference point, R , moving with the constant velocity, v_R , on the reference path has the coordinates (x_R, y_R), and the heading angle, φ_R , satisfies the following equation:

$$\begin{bmatrix}\dot{x}_R\\ \dot{y}_R\\ \dot{\varphi}_R\end{bmatrix}=\begin{bmatrix}\cos\varphi_R & 0\\ \sin\varphi_R & 0\\ 0 & 1\end{bmatrix}\begin{bmatrix}v_R\\ \omega_R\end{bmatrix} \quad (20)$$

The tracking errors can be calculated as follows:

$$\begin{bmatrix}e_1\\ e_2\end{bmatrix}=\begin{bmatrix}\cos\varphi & \sin\varphi\\ -\sin\varphi & \cos\varphi\end{bmatrix}\begin{bmatrix}x_R-x_W\\ y_R-y_W\end{bmatrix} \quad (21)$$

4.2 Controller Design

The goal of designing the controller is to make the kinematic center of the AGV follow a reference point moving with constant velocity along the line. In other words, this means ensuring that:

$$e_i \to 0, (i=1,2)\ as\ t\to\infty$$

The dynamics of the tracking errors can be expressed as follows.

$$\begin{bmatrix}\dot{e}_1\\ \dot{e}_2\end{bmatrix}=\dot{\varphi}\begin{bmatrix}-\sin\varphi & \cos\varphi\\ -\cos\varphi & -\sin\varphi\end{bmatrix}\begin{bmatrix}x_R-x_{W'}\\ y_R-y_{W'}\end{bmatrix}+\begin{bmatrix}\cos\varphi & \sin\varphi\\ -\sin\varphi & \cos\varphi\end{bmatrix}\begin{bmatrix}\dot{x}_R-\dot{x}_{W'}\\ \dot{y}_R-\dot{y}_{W'}\end{bmatrix} \quad (22)$$

Substitute the terms according to equations (19), (20), and (21):

$$\begin{bmatrix}\dot{e}_1\\ \dot{e}_2\end{bmatrix}=\omega_C\begin{bmatrix}e_2\\ -e_1\end{bmatrix}+\begin{bmatrix}\cos\varphi & \sin\varphi\\ -\sin\varphi & \cos\varphi\end{bmatrix}\begin{bmatrix}v_R\cos\varphi_R-v_C\cos\varphi_C+\omega_C d\sin\varphi\\ v_R\sin\varphi_R-v_C\sin\varphi_C-\omega_C d\cos\varphi\end{bmatrix}$$

$$\begin{bmatrix}\dot{e}_1\\ \dot{e}_2\end{bmatrix}=\omega_C\begin{bmatrix}e_2\\ -e_1\end{bmatrix}+\begin{bmatrix}\cos\varphi & \sin\varphi\\ -\sin\varphi & \cos\varphi\end{bmatrix}\begin{bmatrix}\cos\varphi_R & \cos\varphi & d\sin\varphi\\ \sin\varphi_R & -\sin\varphi & -d\cos\varphi\end{bmatrix}\begin{bmatrix}v_R\\ v_C\end{bmatrix}$$

$$\begin{bmatrix}\dot{e}_1\\ \dot{e}_2\end{bmatrix}=\omega_C\begin{bmatrix}e_2\\ -e_1\end{bmatrix}+\begin{bmatrix}\cos(\varphi_R-\varphi) & -1 & 0\\ \sin(\varphi_R-\varphi) & 0 & d\end{bmatrix}\begin{bmatrix}v_R\\ v_C\\ \omega_C\end{bmatrix}$$

$$\begin{bmatrix}\dot{e}_1\\ \dot{e}_2\end{bmatrix}=\begin{bmatrix}e_2\omega_C+v_R\cos\Delta\varphi-v_C\\ -e_1\omega_C+v_R\sin\Delta\varphi+d\omega_C\end{bmatrix} \quad (23)$$

The chosen Lyapunov function is [12, 13]:

$$L=\frac{1}{2}{e_1}^2+\frac{1}{2}{e_2}^2,\begin{cases}L(0)=0\\ L(x)>0, \quad \forall x\end{cases} \quad (24)$$

Derivative of Lyapunov:

$$\dot{L}=e_1\dot{e}_1+e_2\dot{e}_2$$
$$\dot{L}=e_1v_R cos\Delta\varphi-e_1v_C+e_1e_2\omega_C+e_2v_R sin\Delta\varphi-e_1e_2\omega_C-e_2d\omega_C$$
$$\dot{L}=e_1v_R cos\Delta\varphi-e_1v_C+e_2v_R sin\Delta\varphi-e_2d\omega_C$$
$$\dot{L}=e_1(v_R cos\Delta\varphi-v_C)+e_2(v_R sin\Delta\varphi-d\omega_C) \quad (25)$$

The conditions which satisfied the Lyapunov's stability theorem is:

$$\begin{cases}\dot{L}(0)=0\\ \dot{L}(x)<0, \quad \forall x\end{cases}^s$$

Therefore, $\dot{L}$ should in the form of:

$$\dot{L}=-k_1{e_1}^2-k_2{e_2}^2$$

To achieve that, this system of equations must be satisfied:

$$\begin{cases}v_R cos\Delta\varphi-v_C=-k_1e_1\\ v_R sin\Delta\varphi-d\omega_C=-k_2e_2\end{cases}$$

Based on the above equations, we can choose control law:

$$v_C=v_R cos\Delta\varphi+k_1e_1$$
$$\omega_C=\frac{1}{d}v_R sin\Delta\varphi+k_2e_2 \quad (26)$$

Where k_1, k_2 are positive value.

5. Results

Working distance d

To determine the optimal working distance for a 5-sensor line detection array on both white and black surfaces, we conducted a practical test as Fig. 17 using a 3-axis 3D printer with the following setup:

Experiment Procedure:

- Fix the line sensors onto the moving structure of the 3D printer.
- Secure an L-bracket onto the 3D printer table to prevent the sensor array from rotating around the Z-axis, as the rotating axis of the 3D printer is not locked during testing.
- Lower the line sensor array until it touches the measurement surface and record the Z-axis value of the 3D printer.
- Gradually move the 3D printer upwards along the Z-axis in 1mm increments. At each increment, record sensor readings for 2 seconds with a 10ms sampling rate, resulting in 200 readings per sensor at each height.
- Check each height to determine where all 5 sensors provide consistent readings. Continue the test until sensor readings become unstable or inconsistent.
- The results of each distance test on black and white surfaces are as follows:

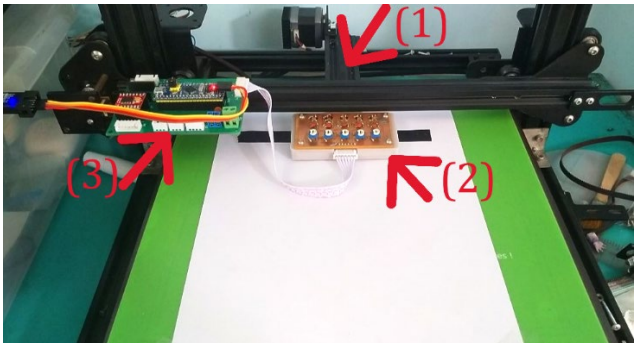

(1) 3D-printer machine CR10, (2) Line Tracking sensor, (3) Circuit

Figure 17. Experiment using 3-axis 3D printer

Black Surface:
We evaluated the average readings of the sensor values on the black surface across different heights. Table 6 describes the results of our testing procedure.

Table 6.
Average value of sensors at each height (black color)

Distance	LED 1	LED 2	LED 3	LED 4	LED 5
0	2324	2564	3347	3414	2954
1	2570	2356	3330	3225	2661
2	3365	3225	3439	3401	3480
3	3201	3110	3143	3229	3434
4	2985	2811	3153	3115	3186
5	3240	2894	3264	3423	3461
6	3115	2704	3282	3261	3358
7	3197	3387	3365	3368	3129
8	3216	3480	3284	3482	3300
9	3309	3286	3269	3183	3175
10	3425	3371	3145	3410	3144
11	3182	3255	3458	3108	3454
12	3466	3405	3149	3336	3295
13	3192	3110	3338	3359	2722

From Fig. 18, we observe that from 7mm to 11mm, all sensors consistently read an average value of 3295 when detecting black. Thus, the ideal working distance for detecting black is between 7mm and 14mm.

White Surface:
Similarly, we obtained the following sample values for the white surface as Table 7.

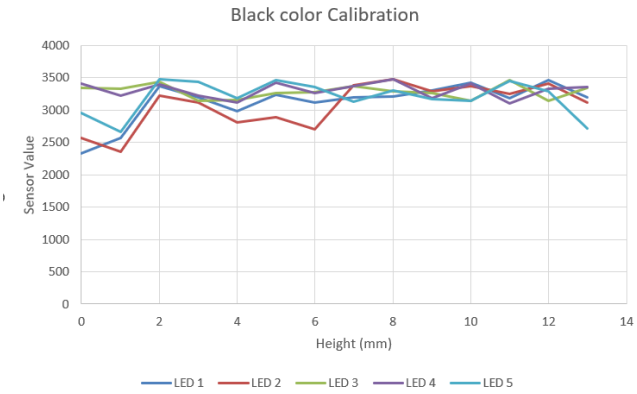

Figure 18. Average value of sensors at each height (Black color)

Table 7.
Average value of sensors at each height (white color)

Distance	LED 1	LED 2	LED 3	LED 4	LED 5
0	3236	1091	2344	2391	363
1	2144	303	306	1884	370
2	1905	294	297	1678	355
3	1665	286	289	1472	340
4	1130	209	200	975	253
5	613	160	178	550	222
6	138	150	146	173	183
7	168	172	179	165	155
8	138	167	172	185	171
9	161	178	180	160	176
10	162	172	188	152	153
11	153	149	181	166	159
12	154	178	155	172	190
13	132	166	179	163	190
14	171	166	179	154	184
15	156	140	185	187	159
16	172	182	163	173	164
17	168	172	145	170	167
18	169	145	153	170	163
19	191	208	190	178	277
20	210	238	237	195	375

21	238	226	237	200	385

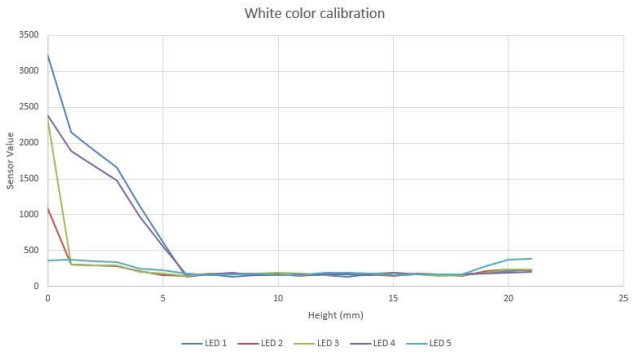

Figure 19. Average value of sensors at each height (White color)

For this test case, the ideal working distance range is from 7mm to 19mm. The optimal working distance for detecting white surfaces is 7-19 mm, and for black surfaces, it is 7-14 mm. The overlapping range of 7-11 mm is ideal for reliable detection of both. A final working distance of 11 mm was chosen to maximize sensor efficiency, ensuring accurate and consistent performance for the line-tracking robot in real-world applications.

Simulation result

Using the kinematic equations in previous section, we can simulate the AGV's motion dynamics in conjunction with its configuration and physical parameters. To control the AGV's motion, the result of our work is described in Fig. 20.

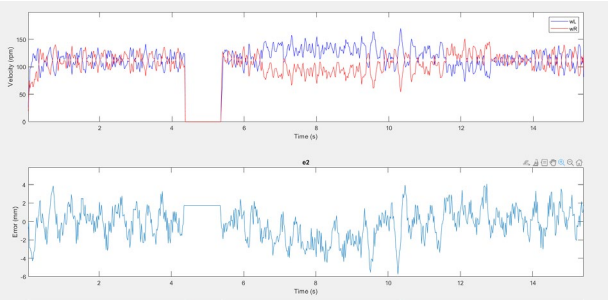

(a)

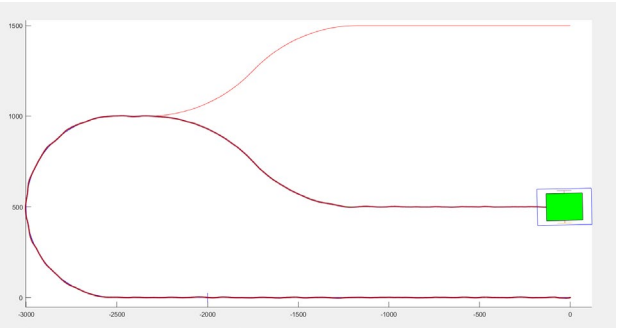

(b)

Figure 20. Tracking simulations; (a) Velocities of two wheels and e_2 graph; (b) AGV motion

The AGV follows a predefined trajectory, and simulated noise is added to the variable e_2 to represent lateral error with environmental uncertainties. This noise introduces realistic variations, mimicking sensor imperfections or environmental disturbances. The motors are modelled using their actual transfer functions, incorporating a previously designed PI controller to regulate their response. This controller ensures stable and accurate velocity adjustments for the left and right wheels. By accounting for these real-world effects, the simulation becomes a closer approximation of practical scenarios, enabling robust performance evaluation.

It is noticed that: we are tracking the centre of the line, and the line is $26mm$ width with tolerance of $\pm 3mm$. For that reason, the allowable e_2 is in the range of $-16mm$ to $16mm$. Hence, our simulation shows that the controller surpasses the requirement with maximum value of e_2 is less than $6\ mm$. Moreover, further tuning will be applied to achieve the best performance.

Result of the real-world validation

The physical realization of the robot closely follows its 3D CAD design, as shown in Fig. 21, which compares the 3D SolidWorks model (left) with the assembled real model (right). The real-world prototype successfully replicates the original shape, size, and layout of the digital design. Notably, the spoke-pattern wheels and their distinct blue coloring are consistent between both models. A placeholder component in the 3D design was replaced with an actual functional device in the final build, and both models share a matte black surface finish, enhancing the robot's clean and professional appearance. This level of detail demonstrates the precision and faithfulness of the fabrication process relative to the design plan.

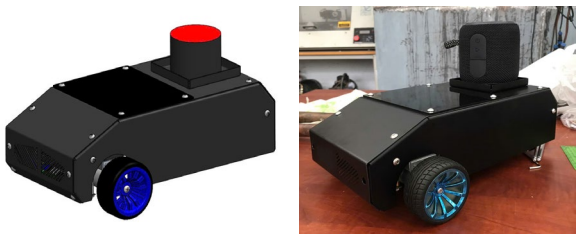

(a) 3D SolidWorks model (b) Real model

Figure 21. 3D model and real model

The functionality of the robot was validated through real-world testing on a predefined track, as illustrated in Fig. 22. The system exhibited strong performance across several key metrics. The stopping

error, measured when the AGV halts at its target point, was approximately 3.5 mm, which is within an acceptable tolerance for warehouse automation applications. The line-tracking capability was also robust, with a maximum lateral deviation of 8.84 mm, as the robot's sensor array maintained consistent tracking of the designated line, even in curved segments.

In terms of dynamic performance, the AGV completed a full course in 25 seconds, including programmed stops, corresponding to an average speed of 0.28 m/s. This outcome demonstrates the effectiveness of the integrated control algorithms and sensor calibration under practical conditions. Overall, the real-world tests confirm that the robot meets its functional requirements and is ready for deployment in educational or industrial automation scenarios.

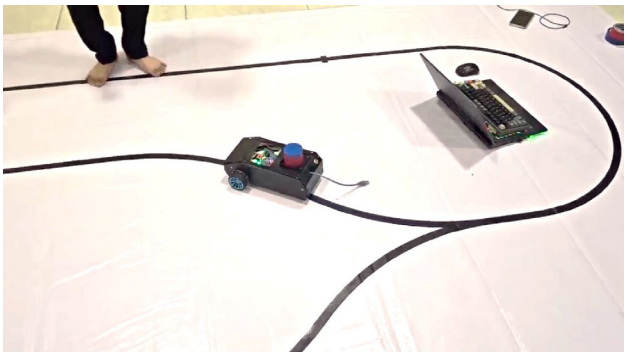

Figure 22. Test runs on the canvas.

6. Conclusion

This study presented the design, development, and implementation of an autonomous line-tracking robot for warehouse logistics applications. The system integrates mechanical, electrical, and software components to achieve autonomous navigation using a color-based line-following algorithm. Through detailed modeling, simulation, and hardware construction, the AGV demonstrated stable motion control, accurate color detection, and consistent line tracking under various conditions. Real-world testing validated the effectiveness of the proposed control algorithms, with satisfactory performance in terms of tracking accuracy, stopping precision, and average speed. The project not only fulfills technical objectives but also serves as a valuable educational tool for students to gain hands-on experience in mechatronic system integration and embedded control.

For future improvements, several directions are proposed. On the mechanical side, the motor mounting assembly will be redesigned using milled positioning grooves to enhance precision and stability. In terms of electrical enhancements, features [14-17] such as LED function indicators, battery level monitoring, and additional control buttons will be integrated to improve usability and system feedback. Algorithmically, further optimization of the control algorithm is needed to reduce computational delay, especially in the Lyapunov-based tracking controller, to ensure robust real-time operation. From a system-wide perspective, future work will aim to increase the AGV's movement speed, reduce both line-following and stopping errors, and extend its operational runtime to meet the demands of more complex logistics environments.

References

[1] Rocha, C., Sousa, I., Ferreira, F., Sobreira, H., Lima, J., Veiga, G., & Moreira, A. P. (2020). Development of an autonomous mobile towing vehicle for logistic tasks. In *Robot 2019: Fourth Iberian Robotics Conference: Advances in Robotics, Volume 1* (pp. 669-681). Springer International Publishing.

[2] Yang, G., Wang, S., Okamura, H., Yasui, T., Ino, S., Okuhata, K., & Mizobuchi, Y. (2025). Autonomous cart docking for transportation robots in complex and dynamic construction environments. *Automation in Construction*, *171*, 105968.

[3] Nguyen, T. P., Nguyen, H., & Ngo, H. Q. T. (2023). Developing and evaluating the context-aware performance of synchronization control in the real-time network protocol for the connected vehicle. *Mobile Networks and Applications*, 1-22.

[4] Tsai, T. H., & Yao, C. H. (2021). A robust tracking algorithm for a human-following mobile robot. *IET Image Processing*, *15*(3), 786-796.

[5] Tran, H. A. M., Ngo, H. Q. T., Nguyen, T. P., & Nguyen, H. (2018, January). Implementation of vision-based autonomous mobile platform to control by A* algorithm. In *2018 2nd International Conference on Recent Advances in Signal Processing, Telecommunications & Computing (SigTelCom)* (pp. 39-44). IEEE.

[6] Ngo, H. Q. T., Nguyen, H., & Nguyen, T. P. (2022). Approaching to the stable transportation based on motion profile phases for material handling system. *Journal of Cleaner Production*, *371*, 133257.

[7] Apriaskar, E., Fahmizal, F., Cahyani, I., & Mayub, A. (2020). Autonomous Mobile Robot based on BehaviourBased Robotic using V-REP Simulator–Pioneer P3-DX Robot. *Jurnal Rekayasa Elektrika*, *16*(1).

[8] Amsters, R., & Slaets, P. (2020). Turtlebot 3 as a robotics education platform. In *Robotics in Education: Current Research and Innovations 10* (pp. 170-181). Springer International Publishing.

[9] Aldarraji, I., Kakei, A. A., Ismaeel, A. G., Tsaramirsis, G., & Patel, A. (2022). Dynamics modeling and motion simulation of a segway robotic transportation system. In *Intelligent Computing Techniques for Smart Energy Systems: Proceedings of ICTSES 2021* (pp. 83-91). Singapore: Springer Nature Singapore.

[10] Garcia, G., Eskandarian, A., Fabregas, E., Vargas, H., & Farias, G. (2025). Cooperative Formation Control of a Multi-Agent Khepera IV Mobile Robots System Using Deep Reinforcement Learning. *Applied Sciences*, *15*(4), 1777.

[11] Phan, L. A. D., & Ngo, H. Q. T. (2023, October). Systematic Review of Smart Robotic Manufacturing in the Context of Industry 4.0. In *International Conference on Context-Aware Systems and Applications* (pp. 19-42). Cham: Springer Nature Switzerland.

[12] Kubo, R., Fujii, Y., & Nakamura, H. (2020). Control Lyapunov function design for trajectory tracking problems of wheeled mobile robot. *IFAC-PapersOnLine*, *53*(2), 6177-6182.

[13] Panahandeh, P., Alipour, K., Tarvirdizadeh, B., & Hadi, A. (2019). A kinematic Lyapunov-based controller to posture stabilization of wheeled mobile robots. *Mechanical Systems and Signal Processing*, *134*, 106319.

[14] Mendez, V., Iberite, F., Shokur, S., & Micera, S. (2021). Current solutions and future trends for robotic prosthetic hands. *Annual Review of Control, Robotics, and Autonomous Systems*, *4*(1), 595-627.

[15] Zou, Y., Kim, D., Norman, P., Espinosa, J., Wang, J. C., & Virk, G. S. (2022). Towards robot modularity—A review of international modularity standardization for service robots. *Robotics and Autonomous Systems*, *148*, 103943.

[16] Alatise, M. B., & Hancke, G. P. (2020). A review on challenges of autonomous mobile robot and sensor fusion methods. *IEEE access*, *8*, 39830-39846.

[17] Rubio, F., Valero, F., & Llopis-Albert, C. (2019). A review of mobile robots: Concepts, methods, theoretical framework, and applications. *International Journal of Advanced Robotic Systems*, *16*(2), 1729881419839596.